Crystal structure of a SLC11 (NRAMP) transporter reveals the basis for transition-metal ion transport

Ehrnstorfer, Ines A; Geerstma, Eric; Pardon, Els; Steyaert, Jan; Dutzler, Raimund

Published in:
Nature Structural and Molecular Biology

Publication date:
2014

Document Version:
Final published version

nature structural & molecular biology

Crystal structure of a SLC11 (NRAMP) transporter reveals the basis for transition-metal ion transport

Ines A Ehrnstorfer[1], Eric R Geertsma[1,4], Els Pardon[2,3], Jan Steyaert[2,3] & Raimund Dutzler[1]

Members of the SLC11 (NRAMP) family transport iron and other transition-metal ions across cellular membranes. These membrane proteins are present in all kingdoms of life with a high degree of sequence conservation. To gain insight into the determinants of ion selectivity, we have determined the crystal structure of *Staphylococcus capitis* DMT (ScaDMT), a close prokaryotic homolog of the family. ScaDMT shows a familiar architecture that was previously identified in the amino acid permease LeuT. The protein adopts an inward-facing conformation with a substrate-binding site located in the center of the transporter. This site is composed of conserved residues, which coordinate Mn^{2+}, Fe^{2+} and Cd^{2+} but not Ca^{2+}. Mutations of interacting residues affect ion binding and transport in both ScaDMT and human DMT1. Our study thus reveals a conserved mechanism for transition-metal ion selectivity within the SLC11 family.

Iron is the most abundant trace element in mammals. As a cofactor of proteins, it plays an important part in different processes ranging from oxygen transport to the catalysis of redox reactions. Owing to the essential role of iron in metabolism and the harm caused by its uncontrolled accumulation in the body, uptake and storage of iron is tightly regulated. In vertebrates, the transport of free iron into the cytoplasm is catalyzed by members of the solute carrier 11 (SLC11) family[1,2]. These secondary active transporters are found in all kingdoms of life, with a high degree of sequence conservation[3]. The human genome encodes two SLC11 transporters (also known as natural resistance–associated macrophage proteins (NRAMPs)): SLC11A1 (NRAMP1)[4] and SLC11A2 (NRAMP2 or DMT1)[5]. Whereas NRAMP1 is expressed in the phagosomes of macrophages, where it has an essential role in host defense against pathogens[6], the divalent metal-ion transporter DMT1 is broadly expressed in the duodenum, kidney, brain, testis and placenta[7]. Malfunction of either protein is associated with iron storage diseases[8] and a decreased resistance against bacterial infections[9]. With respect to function, DMT1 is the most thoroughly characterized family member[10]. The protein catalyzes the cotransport of protons and divalent transition-metal ions such as Fe^{2+}, Mn^{2+} and Cd^{2+}, whereas Zn^{2+} is a poor substrate[5,11]. The alkaline earth metal ions Ca^{2+} and Mg^{2+} are not transported[12]; this is important because their high concentration in the duodenum would interfere with the absorption of Fe^{2+}. DMT1 is the main route for import of Fe^{2+} and potentially also of Mn^{2+} into the human body, but it is also responsible for the uptake of toxic metals such as Cd^{2+} (refs. 13,14).

In bacteria, SLC11 transporters catalyze the import of Mn^{2+} because iron is usually transported either as complex with siderophores or porphyrins[15,16]. Functional characterization and the high sequence homology suggest that bacterial SLC11 homologs share architecture and substrate specificity with their eukaryotic counterparts and thus work by similar transport mechanisms. On the basis of hydropathy analysis, SLC11 transporters are supposed to contain 11 or 12 transmembrane helices with the N terminus located in the cytoplasm[17]. Although SLC11 proteins were recently predicted to share features with a class of transporters including the amino acid transporter LeuT[18–20], detailed structural information on the family has been absent so far.

We were interested in the mechanism of how divalent transition-metal ions are selectively transported across the membrane, whereas other divalent ions, such as Ca^{2+}, are excluded. To address this question, we have determined the structure of a prokaryotic SLC11 transporter, ScaDMT, by X-ray crystallography and have studied its functional properties by isothermal titration calorimetry (ITC) and transport assays. We have also exploited ScaDMT's homology to mammalian family members in our characterization of site-directed mutants of human DMT1 by two-electrode voltage-clamp electrophysiology. Our study reveals a framework for an important class of membrane transporters, and it provides insight into the structural basis of the transition-metal ion selectivity that is conserved within the family.

RESULTS

Functional characterization of ScaDMT

To identify a SLC11 transporter with suitable properties for structural studies, we cloned 105 close prokaryotic homologs with the fragment-exchange (FX) cloning technique[21] and investigated their expression properties in small-volume cultures. Our broad screen allowed us to single out a transporter from the bacterium *S. capitis* (ScaDMT) as a protein with superior expression levels and high stability. ScaDMT is

[1]Department of Biochemistry, University of Zurich, Zurich, Switzerland. [2]Structural Biology Research Center, Vlaams Instituut voor Biotechnologie (VIB), Brussels, Belgium. [3]Structural Biology Brussels, Vrije Universiteit Brussel, Brussels, Belgium. [4]Present address: Institute of Biochemistry, Biocenter, Goethe-University Frankfurt, Frankfurt am Main, Germany. Correspondence should be addressed to R.D. (dutzler@bioc.uzh.ch).

Received 1 May; accepted 19 September; published online 19 October 2014; doi:10.1038/nsmb.2904

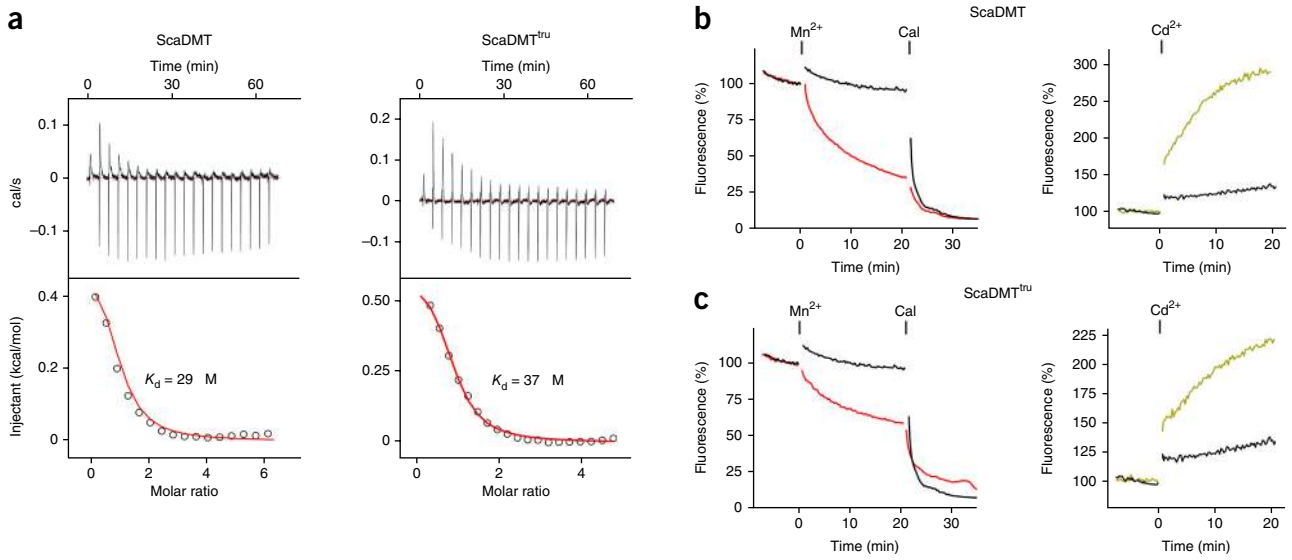

Figure 1 Transition-metal ion binding and transport. (**a**) Cd^{2+} binding to ScaDMT (left) and ScaDMT^{tru} (right), as determined by ITC. Top graphs, heat absorbed upon injection of Cd^{2+} to the experimental chamber containing the respective protein. Bottom graphs, fit of the integrated and corrected heat to a binding isotherm (red line). The exponent *n* was constrained between 0.9 and 1.1. (**b**) Left, ScaDMT-mediated transport of Mn^{2+} into proteoliposomes, showing time-dependent quenching of calcein inside the vesicle, in response to the application of 300 μM Mn^{2+} to the external medium. Addition of Mn^{2+} and the ionophore calcimycin (Cal) is indicated at top. A control trace from liposomes devoid of protein is shown in black. Right, ScaDMT-mediated transport of Cd^{2+} into proteoliposomes, showing time-dependent increase of the fluorescence of fura-2 inside the vesicle, upon addition of 200 μM Cd^{2+} to the external medium. A control trace from liposomes devoid of protein is shown in black. (**c**) ScaDMT^{tru}-mediated transport of Mn^{2+} (left) and Cd^{2+} (right) into proteoliposomes. Procedures are as in **b**.

highly homologous to human DMT1. The protein contains 448 amino acids, of which 37% are identical and 59% are homologous to those in its human counterpart (**Supplementary Fig. 1**). The biggest differences between the two proteins are found in their termini, which are both longer in DMT1. Whereas the 36–amino acid extension on the N terminus of DMT1 is predicted to be unstructured, the 59 additional residues on the C terminus encode an additional transmembrane helix. When purified in the detergent *n*-decyl-β-D-maltoside (DM), ScaDMT is monomeric as determined by multiangle light scattering (MALS; **Supplementary Fig. 2a–e**).

To characterize the interaction of the transporter with divalent cations, we investigated ion binding to the detergent-solubilized protein by ITC. ScaDMT binds the divalent transition-metal ion Cd^{2+}, which has previously been shown to be transported by different pro- and eukaryotic family members[5,16], with micromolar affinity (K_d = 29 ± 10 μM error of fit; **Fig. 1a**). We assayed transport with ion-selective fluorophores after reconstitution of the transporter into liposomes (**Supplementary Fig. 2f**). The time-dependent decrease of the fluorescence after the addition of Mn^{2+} and the fluorescence increase upon addition of Cd^{2+} indicates transport of these ions into proteoliposomes, whereas we observed no fluorescence change for liposomes devoid of protein (**Fig. 1b**). When taken together, our results demonstrate that ScaDMT binds and transports Cd^{2+} and Mn^{2+}. This functional resemblance to mammalian DMT1 underlines the close relationships within the SLC11 family and distinguishes ScaDMT as a valuable model system for understanding transition-metal ion transport.

ScaDMT structure

To learn more about the structural basis of transport, we determined the structure of ScaDMT by X-ray crystallography. Crystallization experiments on the full-length protein allowed us to obtain crystals diffracting to a resolution of 6.5 Å (**Table 1**), which we could not further improve. In an attempt to obtain better-diffracting crystals, we systematically screened shorter constructs of the transporter and generated nanobodies[22] by immunization of llamas and used the nanobodies for cocrystallization with the membrane protein. In the shortest construct, termed ScaDMT^{tru}, we removed 41 amino acids from the N terminus, including 17 residues of the first predicted transmembrane helix (**Supplementary Fig. 1**). This construct was stable, and it transported Cd^{2+} and Mn^{2+} and bound Cd^{2+} with similar affinity (K_d = 37 ± 8 μM) to that of wild type, thus ensuring that the functional properties of the truncated protein were retained (**Fig. 1a,c**). A complex of ScaDMT^{tru} with a nanobody, which recognizes both the full-length and the truncated membrane protein and which promotes dimerization in solution, allowed us to identify crystals with superior diffraction properties that permitted structure determination at 3.1 Å by the selenomethionine single-wavelength anomalous dispersion (SAD) method (**Supplementary Figs. 2** and **3** and **Table 1**). Crystals were of space group $P3_121$ with two copies of the ScaDMT^{tru}–nanobody complex in the asymmetric unit (**Fig. 2a**). Both copies were related by two-fold noncrystallographic symmetry (NCS) and buried 1,190 Å^2 of the combined molecular surface of the membrane protein and 960 Å^2 of the nanobody. Despite the comparably large interaction interface, the two-fold relationship is not likely to represent the oligomeric state of the protein in the membrane because both transporters are tilted with respect to the NCS axis. The nanobody binds to a region exposed to the periplasmic side of the transporter, where it is involved in extensive intermolecular contacts (**Supplementary Fig. 4 a,b**).

ScaDMT contains 11 transmembrane helices, some of which are bent or interrupted by short loops (structure and topology in **Fig. 2**). Its N terminus is located in the cytoplasm, and its C terminus is located on the periplasmic side. The first five α-helices are structurally related to the following five α-helices by an approximate two-fold rotation around an axis located in the center of the membrane and

Table 1 Data collection and refinement statistics

	ScaDMT^{tru}–nanobody	SeMet	ScaDMT^{tru}–nanobody Mn^{2+}	ScaDMT
Data collection				
Wavelength (Å)	1.0	0.9795	1.8940	1.0
Space group	$P3_121$	$P3_121$	$P3_121$	$P3_221$
Cell dimensions				
a, *b*, *c* (Å)	114.4, 114.4, 257.9	114.6, 114.6, 257.6	114.1, 114.1, 257.4	151.8, 151.8, 157.3
α, β, γ (°)	90.0, 90.0, 120.0	90.0, 90.0, 120.0	90.0, 90.0, 120.0	90.0, 90.0, 120.0
Resolution (Å)	50–3.1 (3.3–3.1)	50–3.6 (3.8–3.6)	50–3.4 (3.6–3.4)	50–6.5 (6.7–6.5)
R_{merge}	6.0 (120)	11.2 (142)	8.1 (127)	11.7 (169)
$I / \sigma I$	21.0 (2.1)	19.3 (3.2)	19.0 (2.4)	11.1 (2.1)
Completeness (%)	99.6 (98.2)	100.0 (100.0)	99.9 (100.0)	94.9 (89.5)
Redundancy	9.5 (15.2)	22.0 (22.5)	9.6 (9.4)	12.9 (12.3)
Refinement				
Resolution (Å)	20–3.1		20–3.4	20–6.5
No. reflections	35,850		27,349	3,803
R_{work} / R_{free}	25.0 / 28.5		26.0 / 28.5	27.20 / 33.4
No. atoms				
Protein	7,948		7,948	
Ligand/ion			2	
B factors				
Protein	139		148	
Ligand/ion			194	
r.m.s. deviations				
Bond lengths (Å)	0.003		0.003	
Bond angles (°)	0.75		0.69	

Values in parentheses are for highest-resolution shell. SeMet, selenomethionine.

close to the substrate-binding site are well defined (**Supplementary Fig. 3**). It is noteworthy that in the inward-facing conformation of LeuT, this part of the helix interacts only loosely with the rest of the protein[29]. Electron density of full-length ScaDMT crystallized in the absence of a nanobody at 6.5 Å shows an unaltered conformation with residual electron density for α-helix 1a located at the equivalent position as found in LeuT; this underlines that neither the truncation of the N terminus nor the binding of the nanobody perturbed the ScaDMT^{tru} structure (**Supplementary Fig. 5** and **Table 1**). Although we grew the crystals in conditions containing a high (200 mM) concentration of Ca^{2+}, we did not observe specific binding of this ion in the $2F_o - F_c$ electron density of the refined model and in anomalous difference electron density maps collected at appropriate wavelengths, results suggesting that the protein shows a substrate-free conformation (**Fig. 3c** and **Supplementary Fig. 3d**). The structure of ScaDMT reveals the detailed architecture of SLC11 transporters, and it confirms the relationship between family members and a diverse class of secondary active transporters, as previously postulated from sequence analysis[19,20].

running parallel to its plane (**Fig. 2b,c**). The organization of subdomains as inverted repeats of five transmembrane helices places SLC11 proteins among transporters sharing a conserved protein fold that was initially observed in the amino acid transporter LeuT[18] and was later found in several other transporter families[23–28]. As in these transporters, the first helix of each repeat (i.e., α-helices 1 and 6 in ScaDMT) is unwound in the center of the membrane, thus providing residues for the coordination of the transported substrates. In the crystal structure, the protein adopts an inward-facing conformation that is similar to the corresponding conformations observed for LeuT[29] and the sodium/galactose transporter vSGLT[26] (with r.m.s. deviations of transmembrane helices of 3.2 Å and 3.9 Å respectively; **Supplementary Fig. 4c,d**). Pronounced structural differences are present in the ion-binding region, where the small size of the transported substrate of ScaDMT requires the proximity of coordinating residues. Owing to the truncation at the N terminus, the first half of α-helix 1 is absent, whereas the residues

Ion-binding site

Because the ion binding properties of ScaDMT^{tru} are fully preserved, we used the structure to investigate the interaction with different mono- and divalent cations by X-ray crystallography. Strong anomalous difference density in a data set of a crystal soaked in Mn^{2+} shows binding of the ion to a single site that is accessible from the cytoplasm and located at the unwound parts of α-helices 1 and 6 in the center of the membrane (**Fig. 3a**). Whereas the bound metal ion is well defined, the present resolution of the data does not allow conclusions on the presence of ordered water molecules to be made. Ion binding did not induce any noticeable conformational changes, because the structures of both the complexed and the uncomplexed protein are virtually identical (**Fig. 3b,c**). Mn^{2+} is coordinated by the carbonyl oxygen of the peptide bond connecting residues 223 and 224 at the

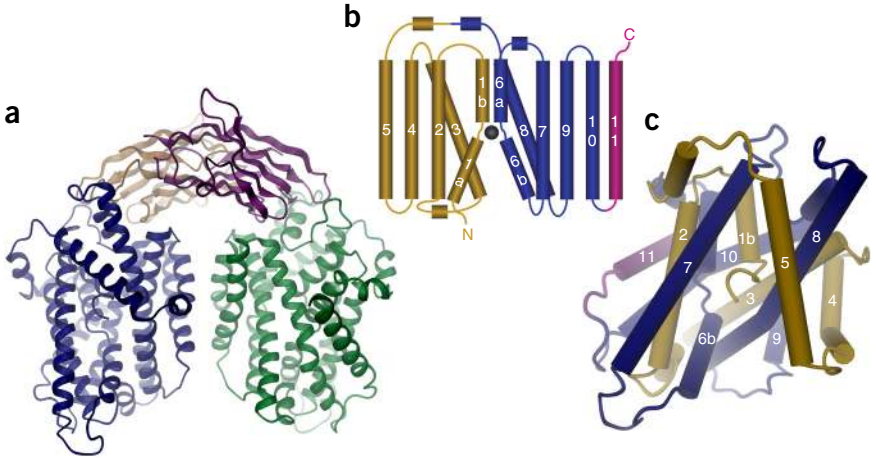

Figure 2 ScaDMT structure. (**a**) Ribbon representation of the dimeric ScaDMT^{tru}–nanobody complex crystallized in Ca^{2+} (ScaDMT^{tru}–Ca^{2+}). The view is perpendicular to the two-fold noncrystallographic symmetry axis. (**b**,**c**) Topology (**b**) and structure (**c**) of ScaDMT^{tru}. The two related halves of the protein are colored in brown and blue, and helix 11 is colored in magenta. Helices are represented as cylinders, and their numbers are labeled. In the topology, the bound ion is indicated by a gray sphere. **Figures 2–4** were prepared with DINO (http://www.dino3d.org/).

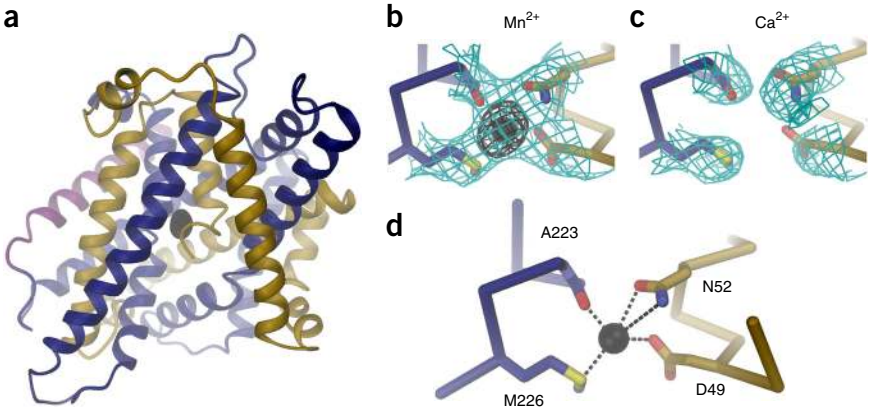

Figure 3 Ion coordination. (**a**) Ribbon representation of a single transporter in the ScaDMT^{tru}–nanobody structure in complex with Mn^{2+} (ScaDMT^{tru}–Mn^{2+}). The color coding of the protein is as in **Figure 2b**. The anomalous difference density of Mn^{2+} (calculated at 3.5 Å and contoured at 13σ) is shown as gray mesh. (**b**–**d**) Close-up view of the ion-binding site of ScaDMT. Sections of the protein are shown as Cα trace with selected main chain and side chain atoms as sticks. The refined Mn^{2+} ion is shown in gray. (**b**) ScaDMT^{tru}–Mn^{2+} with anomalous difference density of Mn^{2+} (contoured at 13σ) shown as gray mesh and the refined $2F_o - F_c$ density (contoured at 1σ) as cyan mesh. (**c**) ScaDMT^{tru}–Ca^{2+}. The refined $2F_o - F_c$ density (contoured at 1σ, cyan) does not show any density of bound ions. (**d**) Transition-metal ion coordination within the binding site. Interactions are indicated by dashed lines. Approximate ion-protein distances: Mn^{2+}-O (backbone, Ala 223), 2.2 Å; Mn^{2+}-S (Met 226), 2.7 Å; Mn^{2+}-O (Asp 49), 2.3 Å; Mn^{2+}-O and Mn^{2+}-N (Asn 52), 2.9 and 3.5 Å, respectively. The Mn^{2+} ion is shown as a gray sphere.

C-terminal end of α-helix 6a; the side chain of Met226 of the same helix; and side chains of Asp49 and Asn52 from the close-by α-helix 1 (**Fig. 3d**). The coordinating atoms, arranged in an approximately planar geometry, provide predominantly hard oxygen ligands along with a soft thioether sulfur ligand. Residues contributing to ion–side chain interactions are strongly conserved within the family, and they are identical in ScaDMT and human DMT1 (**Supplementary Fig. 1**). Our structural studies thus allowed us to identify a conserved binding mode for divalent transition-metal ions that is likely to be shared by all family members.

Because SLC11 transporters are selective for certain transition-metal ions, we were interested in whether the observed transport behavior would be reflected in the ion-coordination properties of the binding site. We hence collected data for ScaDMT^{tru} crystals soaked in solutions containing different mono- and divalent cations, detected by anomalous scattering properties (**Supplementary Table 1**). In that way, we identified Fe^{2+}, Co^{2+}, Ni^{2+}, Cd^{2+} and Pb^{2+} to occupy the same site as Mn^{2+} (**Fig. 4**). We confirmed transport of Mn^{2+}, Cd^{2+}, Co^{2+} and Ni^{2+} in our fluorescence-based transport assay (**Figs. 1b** and **4k**). Cu^{2+} binds to the same location, but its position is shifted (**Fig. 4e**). Zn^{2+}, which follows Cu^{2+} in the periodic table, no longer occupies the same site. Instead, it binds to the aqueous vestibule, where it interacts with the conserved His233, which has been implicated in pH regulation and proton transport (**Fig. 4h**)[11,30]. In transport assays, the presence of excess Zn^{2+} diminishes Mn^{2+} uptake; this suggests that the ion may be transported by ScaDMT or may alternatively act as an inhibitor (**Fig. 4l**). For alkaline earth metal ions, we observed either no binding, as for Ca^{2+}, or observed the ions bound at different locations (**Fig. 4i**,**j**). When added in ten-fold molar excess, none of these ions interfered with Mn^{2+} uptake, thus demonstrating that they are neither high-affinity substrates nor inhibitors of ScaDMT (**Fig. 4l**). The monovalent cation Cs^{+} was bound to sites located at the periphery of the protein, which are unlikely to be relevant for transport (**Supplementary Fig. 3e**). Our data hence indicate that the binding

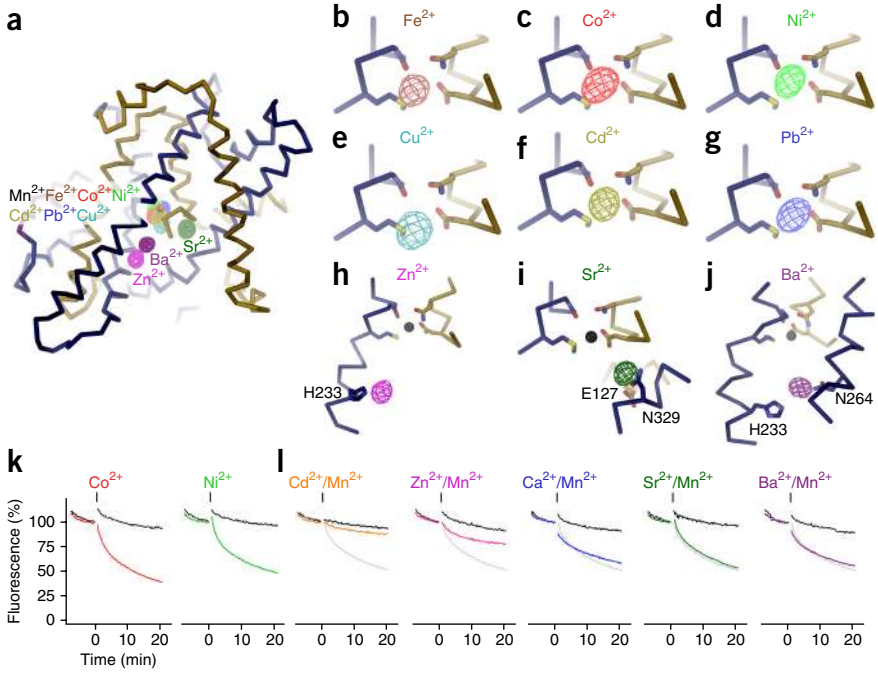

Figure 4 Transition-metal ion selectivity. (**a**) Location of bound ions in different complexes. (**b**–**j**) Close-up views of ion-binding sites with anomalous difference densities (ρ_{ano}) superimposed. (**b**) Fe^{2+} complex (ρ_{ano} calculated at 5 Å and contoured at 6.7σ). (**c**) Co^{2+} complex (5 Å, 7σ). (**d**) Ni^{2+} complex (5 Å, 6.5σ). (**e**) Cu^{2+} complex (6.5 Å, 6σ). (**f**) Cd^{2+} complex (4.5 Å, 10σ). (**g**) Pb^{2+} complex (5 Å, 18σ). (**h**) Zn^{2+} complex (5.5 Å, 7σ). (**i**) Sr^{2+} complex (5 Å, 7.5σ). (**j**) Ba^{2+} complex (5 Å, 9σ). In panels **h**–**j**, the position of Mn^{2+} is indicated by a gray sphere. (**k**) ScaDMT-mediated transport of Co^{2+} and Ni^{2+} into proteoliposomes. Graphs show time-dependent quenching of the fluorophore calcein, that is trapped inside the vesicle, upon addition of 300 μM of the respective ions to the external medium. Traces from liposomes devoid of protein are shown in black. (**l**) ScaDMT-mediated transport of Mn^{2+} into proteoliposomes in the presence of other divalent cations. Graphs show time-dependent quenching of the fluorophore calcein upon addition of 100 μM of Mn^{2+} and either 100 μM Cd^{2+} or 1 mM Zn^{2+}, Ca^{2+}, Sr^{2+} or Ba^{2+} to the external medium. Transport of 100 μM Mn^{2+} is shown in gray for comparison, and traces from liposomes devoid of protein are shown in black.

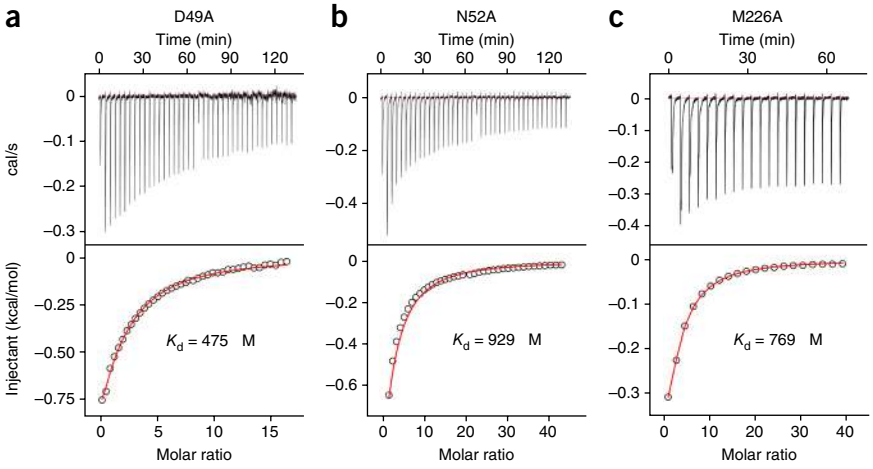

Figure 5 Cd^{2+} binding to ScaDMT binding-site mutants. (**a**–**c**) Cd^{2+} binding to the ScaDMT mutants D49A (**a**), N52A (**b**) and M226A (**c**), as determined by ITC. Top graphs, heat liberated upon injection of Cd^{2+} to the experimental chamber containing the respective protein. Bottom graphs, fit of the integrated and corrected heat to a binding isotherm (red line). The exponent *n* was constrained between 0.9 and 1.1.

of transition-metal ions to a conserved site in the center of the membrane is crucial for ion transport by SLC11 proteins.

Functional investigation of binding-site mutants

To probe the functional relevance of the observed interactions, we studied the effects of mutations of ion-coordinating residues on ScaDMT and human DMT1. Toward this end, we constructed the mutants D49A, N52A and M226A in ScaDMT, to remove residues involved in binding metal ions. After purification and reconstitution, all mutants showed reduced transport activity compared to that of wild-type ScaDMT; this demonstrates that the mutants retained the ability to facilitate transition-metal ion transport at high substrate gradients (**Supplementary Fig. 6**). However, using ITC, we found that the Cd^{2+} binding affinities of the three mutants were decreased by more than an order of magnitude (K_d of 475 ± 38 µM for D49A, 769 ± 27 µM for M226A and 929 ± 151 µM for N52A), as expected for the removal of a coordinating residue (**Fig. 5**). Because the mutation of a single site has a dramatic effect on the binding properties of ScaDMT, we next investigated whether equivalent mutations would show a similar effect on human DMT1. We thus studied DMT1-mediated transport of Cd^{2+} by two-electrode voltage-clamp electrophysiology. We expressed wild type and the mutants D86A, N89A and M265A in *Xenopus laevis* oocytes and recorded the dose-dependent steady-state transport currents with a protocol that was previously used to characterize ion transport by the protein[7]. Whereas the wild-type protein showed robust currents due to Cd^{2+}/H^+ cotransport that saturated with a K_m of 0.3 µM, the K_m of the mutant N89A was shifted by a factor of 19 toward higher concentrations (i.e., to a K_m of 5.6 µM; **Fig. 6a–c**). We observed no Cd^{2+} currents in the mutants D86A and M265A, even at a Cd^{2+} concentration of 1 mM and despite the strong expression of the protein (**Fig. 6d–g** and **Supplementary Data Set 1**). The results thus underline that the same set of residues coordinates divalent transition-metal ions in bacterial and human SLC11 family members.

DISCUSSION

The ScaDMT structure defines the common architecture of the SLC11 (NRAMP) family. These proteins share a conserved molecular scaffold that has previously been observed in different membrane transporters of unrelated sequence. The fold, which is characterized by a topological relationship of protein domains that are oppositely oriented within the membrane, allows for the recognition of substrates in the unwound parts of two symmetry-related helices in the center of the bilayer. In SLC11 transporters, this location contains residues that constitute a promiscuous transition metal ion–binding site. The ion is surrounded predominantly by harder ligands along with the soft sulfur of Met226. Because interacting residues are strongly conserved, it can be assumed that this binding mode is general for the family. The chemical composition of the ion-binding site reflects its preference for transition-metal ions. Mn^{2+} and Fe^{2+} have a tendency to bind to similar sites[31], but, although its thioether group can coordinate both metals, methionine is usually not an interacting residue. However, the

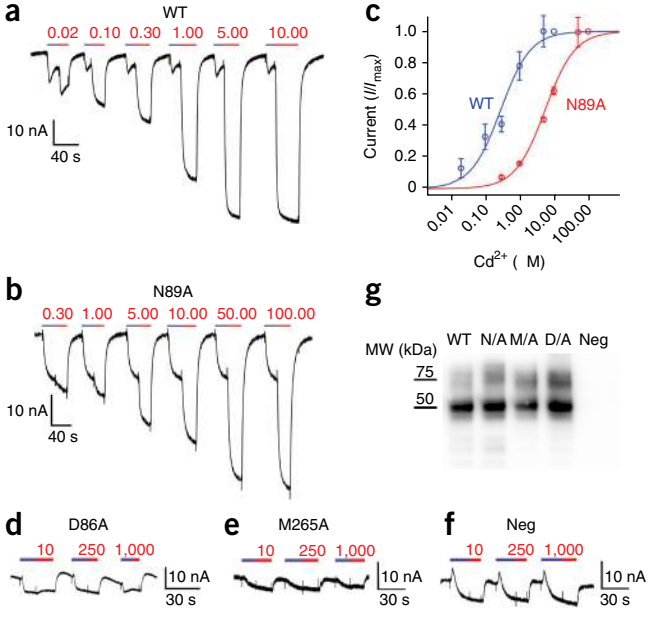

Figure 6 Functional properties of DMT1 binding-site mutants. (**a**,**b**) Concentration dependence of Cd^{2+} transport by human DMT1 expressed in *Xenopus laevis* oocytes. Currents were measured by two-electrode voltage-clamp electrophysiology. Representative current response of wild type (WT) (**a**) and the mutant N89A (**b**) after perfusion of oocytes with solutions containing the indicated amount of Cd^{2+} (in µM) at pH 5.5 (red bar) is shown. In each case, addition of Cd^{2+} was preceded by a pH step from 7.5 to 5.5 (blue bar). Voltage was clamped at −70 mV. (**c**) Dose-response curve of evoked currents in response to Cd^{2+}. Data are averages of either 4 (N52A) or 5 (wild type) independent experiments. Error bars, s.d. The solid lines show a fit to the Michaelis-Menten equation. (**d**–**f**) Representative current response of the binding-site mutants D86A (**d**) and M265A (**e**) and of noninjected oocytes (neg) (**f**) upon application of Cd^{2+}, as observed in 10 (D86A) and 7 (M265A and neg) independent measurements. Protocol is as in **a**. (**g**) Western blot of *Xenopus laevis* oocytes expressing human DMT1 (WT) and the DMT1 binding-site mutants N89A (N/A), M265A (M/A) and D86A (D/A). The positions of the molecular weight (MW) markers are indicated. Noninjected oocytes (neg) are shown as control. Uncropped western blot is shown in **Supplementary Data Set 1**. All oocytes were previously used for electrophysiology experiments.

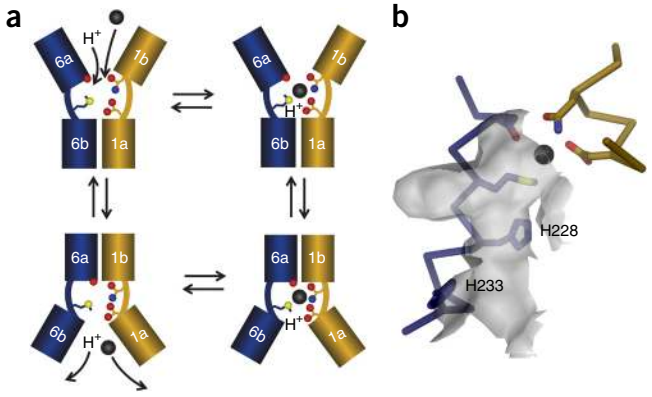

Figure 7 Transport mechanism. (**a**) Schematic drawing of the DMT transport cycle. Binding of a proton and a transition-metal ion to a site that is accessible from the outside is followed by a conformational change of the two halves of α-helices 1 and 6 around a hinge located at the ion-binding region. The rearrangement closes the extracellular pathway and opens an intracellular pathway to the ion-binding site. From this conformation, the two substrates are released into the cytoplasm, and the empty transporter returns to its outward-facing state. (**b**) Structure of the intracellular entry path to the ion-binding site. The bound Mn^{2+} (gray sphere) and the molecular surface around α-helix 6b are shown. Residues of the ion-binding site and two conserved histidines, which have been previously identified as potential H^+ acceptors during proton transport, are displayed as sticks.

fact that Fe^{2+}, Mn^{2+} and Cd^{2+} do frequently interact with the sulfur of cysteine[32,33] suggests that methionine may also be a suitable ligand for these ions. In contrast to transition-metal ions, methionine would be a poor ligand for Ca^{2+}. The binding site thus selects against alkaline earth metal ions, whereas it discriminates poorly between divalent transition-metal ions.

The importance of the observed interactions for binding and transport within the SLC11 family are underlined by mutagenesis, in which truncations of interacting side chains cause a marked decrease in the Cd^{2+} binding affinity of ScaDMT and in which equivalent mutations have a severe impact on Cd^{2+} transport in human DMT1. Because all mutations remove a side chain involved in metal-ion coordination, a similar phenotype can be expected for other transported ions. This would be unlike results from a study on a bacterial SLC30 transporter, in which a single conservative point mutation affected transport of Cd^{2+} but not Zn^{2+} (ref. 34). The binding-site aspartate and asparagine are part of a conserved DPGN motif located in the unwound part of α-helix 1 that was previously identified as a signature for the family[35] and whose mutations cause severe impairment of transport in different family members[36,37]. A similar phenotype was also previously observed for mutations of related residues in α-helix 6 (refs. 36,38).

In ScaDMT, the broad selectivity for transition-metal ions is emphasized by the strong correlation between binding and transport of Mn^{2+}, Fe^{2+}, Co^{2+} and Ni^{2+}, which are neighbors in the periodic table of elements. The next-higher element Cu^{2+} still binds to the same location, although with a slightly shifted position, whereas Zn^{2+} no longer occupies the same site. Our transport assay indicates that Zn^{2+} may act as either an inhibitor or a substrate of ScaDMT. In the latter case, Zn^{2+} would be the only instance that we found of transport being detected for an ion bound to a different region in the protein. Our data also illustrate the discrimination against the alkaline earth metal ions Ca^{2+}, Sr^{2+} and Ba^{2+}, which are not transported by ScaDMT and do not occupy the consensus site. The ion preference of ScaDMT correlates with the properties of DMT1 and other family members, in which Mn^{2+}, Fe^{2+}, Co^{2+} and Cd^{2+} have been shown to be efficiently transported, whereas Ni^{2+}, Cu^{2+} and Zn^{2+} are weaker substrates[5]. As in ScaDMT, alkaline earth metal ions are not transported by DMT1 (ref. 10); this illustrates how Fe^{2+} is selectively absorbed from the duodenum despite the presence of Ca^{2+}, which is several orders of magnitude more abundant[12]. The binding of Cd^{2+} and Pb^{2+} suggests a possible uptake mechanism for these toxic heavy metals[14].

The structure also reveals the location of residues whose mutation in DMT1 causes diseases in humans and rodents (**Supplementary Fig. 7**). The mutation of a conserved glycine residue at the extracellular side of α-helix 4 to arginine leads to severe anemia in mice and rats and has also been shown to be associated with an increased Ca^{2+} permeability of the protein[39]. Four mutations identified in human patients with anemia[40] are scattered in different parts of the protein. Remarkably all mutations affect residues in transmembrane helices remote from the ion-binding region, with all but one of them being conserved in ScaDMT. Because some residues contribute to packing interactions, compromised folding and function of these mutants appear plausible[41].

In the crystal, ScaDMT adopts an inward-facing conformation. Although a single structure provides only a snapshot of the transport cycle, the close structural relationship to the amino acid transporter LeuT and to other proteins sharing a similar protein fold, for which different conformations have been characterized[29,42], allows for the description of a potential outward-facing conformation (**Fig. 7a**). In such a state, the independent movement of both halves of α-helices 1 and 6 around a hinge located in the substrate-binding region would close the intracellular access path and open an extracellular access path to the site, without disrupting the geometry of interacting residues. In this conformation, the same residues probably contribute to the binding of ions from the extracellular environment. However, owing to local structural changes, the affinity in the outward-facing state, which is relevant for scavenging the ion in a physiological context, may be increased, as suggested by the low K_m of transport measured for DMT1.

In DMT1, metal-ion transport is coupled to the movement of protons in the same direction, but the coupling may not be as strict as in other secondary active transporters because uncoupled flows of either of the two substrates have been observed[11]. Although how protons are transported in DMT1 is still unclear, it is noteworthy that two histidines close to the substrate-binding site, which were previously identified to contribute to the pH dependence of transport in pro- and eukaryotic family members[11,30,36], are also conserved in ScaDMT (**Fig. 7b** and **Supplementary Fig. 1**). The presence of these residues suggests that the prokaryotic transporter may share a similar coupling mechanism.

Our study has revealed the structural basis of selectivity in a protein family that has an important role in the transmembrane transport of transition-metal ions in all kingdoms of life. It has thus prepared the ground for detailed investigations of transport mechanisms, which are still poorly understood.

METHODS

Methods and any associated references are available in the online version of the paper.

Accession codes. Coordinates and structure factors for the $ScaDMT^{tru}$–nanobody complex and the $ScaDMT^{tru}$–nanobody Mn^{2+} complex have been deposited in the Protein Data Bank under accession codes 4WGV and 4WGW, respectively.

Note: Any Supplementary Information and Source Data files are available in the online version of the paper.

ACKNOWLEDGMENTS

This research was supported by the Swiss National Science Foundation through the National Centre of Competence in Research TransCure. We thank the staff of the X06SA beamline for support during data collection, B. Blattman and C. Stutz-Ducommun of the Protein Crystallization Center at the University of Zurich for support with crystallization, B. Dreier for help with MALS experiments, the Center for Microscopy and Image Analysis at the University of Zurich for help with freeze-fracture EM, M. Hediger (University of Bern) for providing the cDNA of human DMT1 and E. Beke (Vrije Universiteit Brussel) for help with nanobody selection. All members of the Dutzler laboratory are acknowledged for help in all stages of the project. E.R.G. acknowledges a long-term postdoctoral fellowship from the Human Frontier Science Program (LT-00899/2008). I.A.E. is affiliated with the Biomolecular Structure and Mechanism PhD program of the University of Zurich (UZH) and the Swiss Federal Institute of Technology (ETH) Zurich. Data collection was performed at the X06SA beamline at the Swiss Light Source of the Paul Scherrer Institute.

AUTHOR CONTRIBUTIONS

I.A.E. carried out all experiments except for the initial nanobody selection. E.R.G. supported the high-throughput expression screening and transport assays and initiated nanobody selection by phage display. E.P. performed immunization, cloned and expressed nanobodies and performed the initial selections. J.S. supervised nanobody production. R.D. assisted I.A.E. in structure determination. I.A.E. and R.D. jointly planned the experiments, analyzed the data and wrote the manuscript.

COMPETING FINANCIAL INTERESTS

The authors declare no competing financial interests.

1. Nevo, Y. & Nelson, N. The NRAMP family of metal-ion transporters. *Biochim. Biophys. Acta* **1763**, 609–620 (2006).
2. Montalbetti, N., Simonin, A., Kovacs, G. & Hediger, M.A. Mammalian iron transporters: families SLC11 and SLC40. *Mol. Aspects Med.* **34**, 270–287 (2013).
3. Cellier, M.F., Bergevin, I., Boyer, E. & Richer, E. Polyphyletic origins of bacterial Nramp transporters. *Trends Genet.* **17**, 365–370 (2001).
4. Vidal, S.M., Malo, D., Vogan, K., Skamene, E. & Gros, P. Natural resistance to infection with intracellular parasites: isolation of a candidate for Bcg. *Cell* **73**, 469–485 (1993).
5. Illing, A.C., Shawki, A., Cunningham, C.L. & Mackenzie, B. Substrate profile and metal-ion selectivity of human divalent metal-ion transporter-1. *J. Biol. Chem.* **287**, 30485–30496 (2012).
6. Vidal, S.M., Pinner, E., Lepage, P., Gauthier, S. & Gros, P. Natural resistance to intracellular infections: Nramp1 encodes a membrane phosphoglycoprotein absent in macrophages from susceptible (Nramp1 D169) mouse strains. *J. Immunol.* **157**, 3559–3568 (1996).
7. Gunshin, H. *et al.* Cloning and characterization of a mammalian proton-coupled metal-ion transporter. *Nature* **388**, 482–488 (1997).
8. Beaumont, C. *et al.* Two new human DMT1 gene mutations in a patient with microcytic anemia, low ferritinemia, and liver iron overload. *Blood* **107**, 4168–4170 (2006).
9. Johnson, E.E. & Wessling-Resnick, M. Iron metabolism and the innate immune response to infection. *Microbes Infect.* **14**, 207–216 (2012).
10. Shawki, A., Knight, P.B., Maliken, B.D., Niespodzany, E.J. & Mackenzie, B.H. H^+-coupled divalent metal-ion transporter-1: functional properties, physiological roles and therapeutics. *Curr. Top. Membr.* **70**, 169–214 (2012).
11. Mackenzie, B., Ujwal, M.L., Chang, M.H., Romero, M.F. & Hediger, M.A. Divalent metal-ion transporter DMT1 mediates both H^+ -coupled $Fe2^+$ transport and uncoupled fluxes. *Pflugers Arch.* **451**, 544–558 (2006).
12. Shawki, A. & Mackenzie, B. Interaction of calcium with the human divalent metal-ion transporter-1. *Biochem. Biophys. Res. Commun.* **393**, 471–475 (2010).
13. Au, C., Benedetto, A. & Aschner, M. Manganese transport in eukaryotes: the role of DMT1. *Neurotoxicology* **29**, 569–576 (2008).
14. Bressler, J.P., Olivi, L., Cheong, J.H., Kim, Y. & Bannona, D. Divalent metal transporter 1 in lead and cadmium transport. *Ann. NY Acad. Sci.* **1012**, 142–152 (2004).
15. Guerinot, M.L. Microbial iron transport. *Annu. Rev. Microbiol.* **48**, 743–772 (1994).
16. Makui, H. *et al.* Identification of the *Escherichia coli* K-12 Nramp orthologue (MntH) as a selective divalent metal ion transporter. *Mol. Microbiol.* **35**, 1065–1078 (2000).
17. Czachorowski, M., Lam-Yuk-Tseung, S., Cellier, M. & Gros, P. Transmembrane topology of the mammalian Slc11a2 iron transporter. *Biochemistry* **48**, 8422–8434 (2009).
18. Yamashita, A., Singh, S.K., Kawate, T., Jin, Y. & Gouaux, E. Crystal structure of a bacterial homologue of Na^+/Cl^--dependent neurotransmitter transporters. *Nature* **437**, 215–223 (2005).
19. Cellier, M.F. Nramp: from sequence to structure and mechanism of divalent metal import. *Curr. Top. Membr.* **69**, 249–293 (2012).
20. Cellier, M.F. Nutritional immunity: homology modeling of Nramp metal import. *Adv. Exp. Med. Biol.* **946**, 335–351 (2012).
21. Geertsma, E.R. & Dutzler, R. A versatile and efficient high-throughput cloning tool for structural biology. *Biochemistry* **50**, 3272–3278 (2011).
22. Pardon, E. *et al.* A general protocol for the generation of Nanobodies for structural biology. *Nat. Protoc.* **9**, 674–693 (2014).
23. Schulze, S., Koster, S., Geldmacher, U., Terwisscha van Scheltinga, A.C. & Kuhlbrandt, W. Structural basis of Na^+-independent and cooperative substrate/product antiport in CaiT. *Nature* **467**, 233–236 (2010).
24. Ressl, S., Terwisscha van Scheltinga, A.C., Vonrhein, C., Ott, V. & Ziegler, C. Molecular basis of transport and regulation in the Na^+/betaine symporter BetP. *Nature* **458**, 47–52 (2009).
25. Weyand, S. *et al.* Structure and molecular mechanism of a nucleobase-cation-symport-1 family transporter. *Science* **322**, 709–713 (2008).
26. Faham, S. *et al.* The crystal structure of a sodium galactose transporter reveals mechanistic insights into Na^+/sugar symport. *Science* **321**, 810–814 (2008).
27. Gao, X. *et al.* Structure and mechanism of an amino acid antiporter. *Science* **324**, 1565–1568 (2009).
28. Fang, Y. *et al.* Structure of a prokaryotic virtual proton pump at 3.2 Å resolution. *Nature* **460**, 1040–1043 (2009).
29. Krishnamurthy, H. & Gouaux, E. X-ray structures of LeuT in substrate-free outward-open and apo inward-open states. *Nature* **481**, 469–474 (2012).
30. Lam-Yuk-Tseung, S., Govoni, G., Forbes, J. & Gros, P. Iron transport by Nramp2/DMT1: pH regulation of transport by 2 histidines in transmembrane domain 6. *Blood* **101**, 3699–3707 (2003).
31. Edward, R.A., Whittaker, M.M., Whittaker, J.W., Jameson, G.B. & Baker, E.N. Distinct metal environment in Fe-substituted manganese superoxide dismutatse provides a structural basis of metal specificity. *J. Am. Chem. Soc.* **120**, 9684–9685 (1998).
32. Qi, W. & Cowan, J.A. Structural, mechanistic and coordination chemistry of relevance to the biosynthesis of iron-sulfur and related iron cofactors. *Coord. Chem. Rev.* **255**, 688–699 (2011).
33. Freisinger, E. & Vasak, M. Cadmium in metallothioneins. *Met. Ions. Life Sci.* **11**, 339–371 (2013).
34. Hoch, E. *et al.* Histidine pairing at the metal transport site of mammalian ZnT transporters controls $Zn2^+$ over $Cd2^+$ selectivity. *Proc. Natl. Acad. Sci. USA* **109**, 7202–7207 (2012).
35. Cellier, M. *et al.* Nramp defines a family of membrane proteins. *Proc. Natl. Acad. Sci. USA* **92**, 10089–10093 (1995).
36. Courville, P. *et al.* Solute carrier 11 cation symport requires distinct residues in transmembrane helices 1 and 6. *J. Biol. Chem.* **283**, 9651–9658 (2008).
37. Haemig, H.A. & Brooker, R.J. Importance of conserved acidic residues in mntH, the Nramp homolog of *Escherichia coli*. *J. Membr. Biol.* **201**, 97–107 (2004).
38. Haemig, H.A., Moen, P.J. & Brooker, R.J. Evidence that highly conserved residues of transmembrane segment 6 of *Escherichia coli* MntH are important for transport activity. *Biochemistry* **49**, 4662–4671 (2010).
39. Xu, H., Jin, J., DeFelice, L.J., Andrews, N.C. & Clapham, D.E. A spontaneous, recurrent mutation in divalent metal transporter-1 exposes a calcium entry pathway. *PLoS Biol.* **2**, E50 (2004).
40. Iolascon, A. & De Falco, L. Mutations in the gene encoding DMT1: clinical presentation and treatment. *Semin. Hematol.* **46**, 358–370 (2009).
41. Courville, P., Chaloupka, R. & Cellier, M.F. Recent progress in structure-function analyses of Nramp proton-dependent metal-ion transporters. *Biochem. Cell Biol.* **84**, 960–978 (2006).
42. Forrest, L.R. *et al.* Mechanism for alternating access in neurotransmitter transporters. *Proc. Natl. Acad. Sci. USA* **105**, 10338–10343 (2008).

ONLINE METHODS

Cloning and expression screening of prokaryotic DMT homologs. For expression screening, the genes of 105 prokaryotic SLC11 transporters were amplified from their respective genomic DNA and cloned into the arabinose-inducible expression vectors pBXNH3, pBXC3H and pBXC3GH with fragment-exchange (FX) cloning[21]. Primers were designed in an automated fashion with a Python script available online (http://www.fxcloning.org/). *Escherichia coli* MC1061 (ref. 43) was used as a cloning and expression strain. Expression and extraction properties were initially investigated in small-scale cultures. For that purpose, cells containing the respective constructs were grown in 24-well plates in terrific broth (TB) and induced with three different arabinose concentrations. Proteins with a periplasmic C terminus were detected by western blot with an anti-polyhistidine antibody (Roche 11965985001, at 1:1,000 dilution). Validation of the antibody can be found on the manufacturer's website. Proteins with a cytoplasmic C terminus were expressed as GFP fusion constructs and detected by the fluorescence of GFP as measured in whole cells and by in-gel fluorescence in SDS-PAGE. Stability and monodispersity of GFP constructs was monitored by fluorescence size-exclusion chromatography (FSEC) before purification[44]. For constructs with a periplasmic C terminus, these properties were assessed by SEC after scale-up and purification. As a result of these experiments, ScaDMT (from *S. capitis* DSM 20326) was identified as a promising candidate for structural studies. For large-scale expression and purification, ScaDMT and all modified constructs were fused to a C-terminal His_{10} tag separated from the protein by a human rhinovirus (HRV) 3C protease–cleavage site. Truncations and mutants of ScaDMT were prepared by PCR and the FX cloning method. For crystallization purposes, shortened constructs of ScaDMT were prepared by systematic truncation of both termini by increments of four residues and investigated by purification. In that way, ScaDMT^{tru}, lacking 41 amino acids at the N terminus was identified as the shortest well-behaved construct.

Protein expression and purification. The genes encoding ScaDMT and ScaDMT^{tru} were cloned into the pBXC3H vector, where they were fused to a C-terminal His_{10} tag separated by a HRV 3C protease–cleavage site. Cells were grown by fermentation of 9- to 18-l cultures in TB medium to an OD_{600} of 2.5. Protein expression was induced by addition of 0.005% (w/v) arabinose at 25 °C. The temperature was decreased to 18 °C for overnight expression. All of the following steps were carried out at 4 °C. Cells were harvested by centrifugation and lysed in buffer A (50 mM potassium phosphate, pH 7.5, and 150 mM NaCl) with a custom-made cell disruptor. The lysate was cleared by low-spin centrifugation. Membranes were harvested by ultracentrifugation. For membrane-protein extraction, vesicles were suspended in buffer A containing 10% (w/v) glycerol and 1–2% (w/v) DM (Anatrace). After centrifugation, the protein was purified by immobilized metal affinity chromatography (IMAC). For cleavage of the His_{10} tag, the sample was incubated with HRV 3C protease (at a molar ratio of 5:1) for 2 h during dialysis into buffer B (20 mM HEPES, pH 7.5, 150 mM NaCl, 5% (w/v) glycerol, and 0.25% (w/v) DM). Histidine-tagged HRV 3C protease was subsequently removed by binding to Ni-NTA resin. The cleaved protein was concentrated and subjected to size-exclusion chromatography (SEC) on a Superdex S200 column (GE Healthcare) equilibrated in 10 mM HEPES, pH 7.5, 150 mM NaCl, and 0.25% (w/v) DM. The peak fractions were pooled and immediately used for experiments. Protein complexes were prepared by incubation of the SEC-purified and concentrated transporter with the SEC-purified and concentrated nanobody (supplemented with 0.25% (w/v) DM) at a molar ratio of 1:1.3 for 5 min. The complex was subjected to SEC (GE Healthcare). Protein–nanobody complexes were subsequently concentrated and used for crystallization. For preparation of crystals used for structure determination, DM was exchanged to *n*-nonyl-β-D-maltopyranoside (NM, 0.84% (w/v)) in SEC.

Generation of nanobodies. ScaDMT-specific nanobodies were generated essentially as previously described[22]. In brief, one llama (*Lama glama*) was immunized six times with 50 µg of detergent-solubilized ScaDMT (in 0.25% DM). 4 d after the final antigen boost, peripheral blood lymphocytes were extracted, and their RNA was purified and converted into cDNA via reverse-transcription PCR . The nanobody repertoire was cloned into the phage-display vector pMESy4 containing a C-terminal His_6 tag followed by the CaptureSelect C tag (Glu-Pro-Glu-Ala). 12 nanobody families that bound to ScaDMT or ScaDMT^{tru} were identified in two rounds of biopanning. Targets were coated directly on a solid phase or immobilized via neutravidin capturing. Antigen-bound phages were recovered from antigen-coated wells without affecting phage infectivity by proteolysis with trypsin. After two rounds of selection, ELISAs were performed on periplasmic extracts of 48 individual colonies of each selection condition to screen for ScaDMT-specific nanobodies. Nb6616, which was crystallized in complex with ScaDMT^{tru} for structure determination, was selected by solid phase–coated ScaDMT^{tru} and neutravidin-captured biotinylated full-length ScaDMT.

Nanobody expression and purification. The 16 nanobodies identified in the initial selection were recloned into an arabinose-inducible expression vector containing an N-terminal pelB leader sequence, a His_{10} tag, a maltose-binding protein (MBP) tag and a HRV 3C protease site. *E. coli* MC1061 cells were grown in a fermenter in TB medium at 37 °C until an OD_{600} of ~3–4 was reached. Expression was induced by addition of 0.02% (w/v) arabinose, and cells were incubated for 6 h at 37 °C. Cells were harvested by centrifugation and lysed with a custom-made cell disruptor. All of the following steps were carried out at 4 °C. The lysate was cleared by centrifugation at 210,000*g*. IMAC was performed as described for the transporter, except that no detergent was used during purification. Peak fractions were mixed with HRV 3C protease at an 8:1 molar ratio and dialyzed against dialysis buffer overnight. Protease and MBP were removed by binding to Ni-NTA. The cleaved nanobody was concentrated by centrifugation (Millipore, MWCO 3 kDa) and subjected to SEC. Peak fractions were pooled and used for experiments.

Expression of selenomethionine-labeled protein. For preparation of selenomethionine-labeled protein, an overnight culture of ScaDMT^{tru} grown in TB medium was diluted 1:100 into 30 l M9 medium supplemented with trace elements, Kao and Michayluk Vitamin solution (Sigma), 0.75% glycerol and 100 mg/l ampicillin. Cells were grown in shaking culture at a starting temperature of 37 °C. The temperature was gradually decreased over 5 h to 24 °C until an OD_{600} of 0.6 was reached. Amino acids L-lysine, L-threonine, and L-phenylalanine (each at a concentration of 125 mg/l) and L-leucine, L-isoleucine and L-valine (each at a concentration of 62.5 mg/l) were added to the culture to inhibit the methionine synthesis pathway[45]. Depletion of free L-methionine was performed for 1 h, and this was followed by addition of 50 mg/l L-selenomethionine. 1 h later, expression was induced by addition of 0.004% (w/v) arabinose. For overnight expression, the temperature was further decreased to 18 °C. Cells were harvested by centrifugation and lysed by sonication. Extraction was started from cleared lysate by addition of 1.5% DM (Anatrace). Purification and crystallization of the ScaDMT^{tru}–NB complex was carried out as described in Online Methods.

Crystallization. ScaDMT (5–10 mg/ml) was crystallized in sitting drops at 4 °C. The best crystals diffracting to 6.5 Å were obtained for protein purified in DM in reservoir solution containing 90 mM MES, pH 6.0, 90 mM NaCl, 200 mM $CaCl_2$ and 26–30% PEG 400 (v/v). Crystals of the ScaDMT^{tru}–nanobody complex (in NM) used for structure determination grew at 4 °C from a reservoir solution containing 50 mM HEPES, pH 7.4, 200 mM $CaCl_2$, and 22–26% PEG 400 (v/v). For cryoprotection, the PEG concentration was increased stepwise to 36%, and crystals were flash frozen in liquid propane. For generation of ion complexes, crystals were soaked for 1 min in freshly prepared solutions in which Ca^{2+} was replaced stepwise by the respective cation.

Structure determination. All data sets were collected on frozen crystals on the X06SA beamline at the Swiss Light Source of the Paul Scherrer Institut on a PILATUS 6M detector (Dectris; **Table 1** and **Supplementary Table 1**). The data were indexed, integrated and scaled with XDS[46] and further processed with CCP4 programs[47]. The structure of the ScaDMT^{tru}–nanobody complex was determined by the SAD method with data collected from crystals containing a selenomethionine-derivatized transporter. The selenium sites were identified with SHELX C and D[48,49]. Selenium sites were refined in SHARP[50], and phases were improved by solvent flattening and extended to 3.1 Å by two-fold NCS symmetry averaging with the program DM[51]. The model was built in O[52] and COOT[53] and initially refined, maintaining strict two-fold NCS constraints in CNS[54]. In later stages, the strict constraints were loosened, and restrained individual *B* factors and TLS parameters were refined in PHENIX[55]. *R* and R_{free} were monitored throughout. R_{free} was calculated by selecting 5% of the reflection data that were omitted in refinement. The final model has R/R_{free} values of 25.0% and 28.5%, good geometry and no residues in disallowed regions of the Ramachandran plot (**Table 1**). Data of ion complexes were collected at appropriate wavelengths to maximize the anomalous scattering of the bound ions (**Table 1** and **Supplementary Table 1**). The structure of the

ScaDMT^{tru}– nanobody Mn^{2+} complex at 3.4 Å was refined in PHENIX as described for the ScaDMT^{tru}–NB complex. For all other ion complexes, the refined structure of the ScaDMT^{tru}–NB Mn^{2+} complex served as start model, and coordinates were subsequently improved by rigid-body refinement in PHENIX. The structure of ScaDMT at 6.5 Å was determined by molecular replacement with Phaser[56] and improved by rigid-body refinement in PHENIX (**Table 1**).

Preparation of proteoliposomes. Proteoliposomes containing ScaDMT were prepared as described in ref. 57. In brief, *E. coli* polar lipid extract (Avanti Polar Lipids) was mixed with L-α phosphatidylcholine (from egg yolk, Sigma) both dissolved in chloroform at a w/w ratio of 3:1. Lipids were dried in a rotary evaporator and subsequently resuspended and sonicated in buffer containing 20 mM HEPES, pH 7.5, and 100 mM KCl. Large unilamellar vesicles were formed by alternating freeze-thaw cycles followed by extrusion through a 400-nm polycarbonate filter (Avestin, LiposoFast-Basic). Liposomes were diluted to 4 mg/ml and destabilized by addition of Triton X-100. The protein sample was incubated with destabilized liposomes at a protein-to-lipid ratio of 1:40 (w/w). Detergent was removed by addition of Bio-Beads SM-2 (Bio-Rad). Proteoliposomes were harvested by centrifugation for 30 min at 236,000*g*, resuspended in buffer and stored in liquid nitrogen.

Freeze-fracture electron microscopy. Freeze-fracture EM was used to monitor the incorporation of the protein into liposomes. For that purpose, proteoliposomes were initially subjected to two freeze-thaw cycles and applied on a copper grid. The grid was subsequently sandwiched between two aluminum specimen carriers and frozen in liquid nitrogen with a high-pressure freezing system (Leica EM HPM100). Glycerol (final concentration 10% (w/v)) was added to the sample if necessary. Freeze fracturing and shadowing were performed on a Leica EM BAF060 at −150 °C under high vacuum. The samples were coated with a 2.5-nm carbon/platinum layer at an angle of 45° immediately after fracturing and were subsequently coated with 20 nm carbon at an angle of 90°. Replicas were imaged with a Philips CM100 transmission electron microscope equipped with a Gatan Orius CCD camera.

Fluorescence-based transport assay. For transport assays, proteoliposomes were mixed with buffer C containing 25 mM HEPES, pH 7.5, 200 mM KCl and either 250 μM calcein or fura-2 (Invitrogen), sonicated, subjected to three freeze-thaw cycles and finally extruded through a 400-nm polycarbonate filter (Avestin, LiposoFast-Basic). Subsequently proteoliposomes were harvested by centrifugation and washed by resuspension in ten volumes of assay buffer without fluorophore. In total, three wash steps were performed. Control liposomes without protein were prepared with the same procedure. The assay was started by dilution of the sample to 2 mg lipid/ml in 100 μl buffer C in a black 96-well plate. Uptake of Me^{2+} into liposomes was monitored by the change of the fluorescence signal in a fluorimeter (Tecan Infinite M1000, calcein, λ_{ex} = 492 nm/λ_{em} = 518 nm; fura-2, λ_{ex} = 335 nm/λ_{em} = 505 nm). After stabilization of the fluorescence signal, ions were added, and fluorescence was recorded every 15 s. After 20 min, Me^{2+} ions were equilibrated by addition of the ionophore calcimycin, which acts as a Me^{2+}/H^{+} exchanger. Experiments with Fe^{2+}, Cu^{2+} and Pb^{2+} were incompatible with the described procedure.

Isothermal titration calorimetry. Proteins were purified in DM as described above and dialyzed overnight against buffer D (25 mM HEPES, pH 7.5, 150 mM NaCl and 0.25% (w/v) DM). ITC experiments were performed with a MicroCal ITC200 system (GE Healthcare) at 6 °C. The sample cell was filled with protein solution at a concentration between 110 and 180 μM. The solution used for titration was prepared by addition of Cd^{2+} to buffer D at a concentration of 4–25 mM. Cd^{2+} was added to the protein by sequential injections of 2-μl aliquots followed by 200 s of equilibration after each injection. For the determination of the background, the same experiment was carried out, except that the protein solution was replaced by buffer D. For analysis, the heat released by each injection was integrated, and the background was subtracted with NITPIC[58]. The data were fit to the Wiseman isotherm with the Origin ITC analysis package. The exponent *n* was constrained between 0.9 and 1.1. ITC experiments were performed at least twice for each protein, with similar results.

Multiangle light scattering. MALS experiments were carried out at 20 °C on an HPLC system (Agilent 1100) connected to an Eclipse 3 system equipped with a miniDAWN TREOS MALS detector and an Optilab T-rEX refractometer (Wyatt Technology). 50 μg of purified protein (at 1 mg/ml) was injected onto a Superdex S200 column (GE Healthcare) equilibrated in 10 mM HEPES, pH 7.5, 150 mM NaCl, and 0.25% (w/v) DM. Molecular weights and s.d. were determined with the Astra package (Astra 6.0, Wyatt Technology).

Two-electrode voltage-clamp experiments. The genes encoding human DMT1 (isoform 3, splice variant 1A–IRE) and the mutants D86A, N89A and M265A (numbering of residues according to the reference sequence isoform 1) were cloned into a pTLN vector[59]. The plasmid was linearized with MluI and was used to prepare capped complementary mRNA with the mMessage mMachine kit (Ambion). mRNA was purified with the RNeasy kit (Qiagen) and injected into defolliculated *Xenopus laevis* oocytes (50 ng/oocyte). Oocytes were incubated at 16 °C for 2–4 d before two-electrode voltage-clamp experiments were performed. Currents were recorded at −70 mV on an OC-725B oocyte clamp (Warner Instrument Corp). Data were sampled at 2 kHz and filtered at 50 Hz. During experiments, oocytes were perfused with high-pH solution containing 100 mM NaCl, 1 mM KCl, 0.6 mM $CaCl_2$, 1 mM $MgCl_2$, and 10 mM HEPES, pH 7.4. Measurements of Cd^{2+}-induced transport currents were preceded by a change into low-pH solution (in which HEPES was replaced by 10 mM MES, pH 5.5) and then a change into low-pH solution containing the desired concentration of $CdCl_2$ (0.02–1,000 μM). Expression of DMT1 was confirmed by western blot with a mouse anti-human SLC11A2 antibody (Sigma WH0004891M1, at 1:5,000 dilution) and a goat anti-mouse antibody coupled to horseradish peroxidase (Dianova 115-035-146, at 1:10,000 dilution) for detection. Validation of antibodies used in the assay can be found on the respective manufacturers' websites.

***Xenopus laevis* oocyte membrane preparation for western blot analysis.** After two-electrode voltage-clamp recording, oocytes were homogenized in Barth's solution containing protease inhibitors (Complete EDTA-free, Roche). Cell debris was removed by centrifugation at 500*g*. Membranes were subsequently harvested by centrifugation at 10,000*g* at 4 °C and resuspended in buffer containing 10 mM HEPES, pH 7.5 and 100 mM NaCl. For extraction, 2% (w/v) *n*-dodecyl-β-D-maltopyranoside (Anatrace) was added, and the samples were incubated on ice for 1 h. Insoluble material was pelleted by centrifugation at 500*g*, and the supernatant was used for western blot analysis.

43. Casadaban, M.J. & Cohen, S.N. Analysis of gene control signals by DNA fusion and cloning in *Escherichia coli*. *J. Mol. Biol.* **138**, 179–207 (1980).
44. Kawate, T. & Gouaux, E. Fluorescence-detection size-exclusion chromatography for precrystallization screening of integral membrane proteins. *Structure* **14**, 673–681 2006).
45. Van Duyne, G.D., Standaert, R.F., Karplus, P.A., Schreiber, S.L. & Clardy, J. Atomic structures of the human immunophilin FKBP-12 complexes with FK506 and rapamycin. *J. Mol. Biol.* **229**, 105–124 (1993).
46. Kabsch, W. Automatic processing of rotation diffraction data from crystals of initially unknown symmetry and cell constants. *J. Appl. Crystallogr.* **26**, 795–800 (1993).
47. Collaborative Computational Project, Number 4. The CCP4 Suite: programs for X-ray crystallography. *Acta Crystallogr. D Biol. Crystallogr.* **50**, 760–763 (1994).
48. Schneider, T.R. & Sheldrick, G.M. Substructure solution with SHELXD. *Acta Crystallogr. D Biol. Crystallogr.* **58**, 1772–1779 (2002).
49. Pape, T. & Schneider, T.R. HKL2MAP: a graphical user interface for phasing with SHELX programs. *J. Appl. Crystallogr.* **37**, 843–844 (2004).
50. De La Fortelle, E. & Bricogne, G. Maximum-likelihood heavy-atom parameter refinement for multiple isomorphous replacement and multiwavelength anomalous diffraction methods. *Methods Enzymol.* **276**, 472–494 (1997).
51. Cowtan, K. dm: an automated procedure for phase improvement by density modification. *Joint CCP4 and ESF-EACBM Newslett. Protein Crystallogr.* **31**, 34–38 (1994).
52. Jones, T.A., Zou, J.Y., Cowan, S.W. & Kjeldgaard, M. Improved methods for building protein models in electron density maps and the location of errors in these models. *Acta Crystallogr. A* **47**, 110–119 (1991).
53. Emsley, P. & Cowtan, K. Coot: model-building tools for molecular graphics. *Acta Crystallogr. D Biol. Crystallogr.* **60**, 2126–2132 (2004).
54. Brünger, A.T. *et al.* Crystallography & NMR system: a new software suite for macromolecular structure determination. *Acta Crystallogr. D Biol. Crystallogr.* **54**, 905–921 (1998).
55. Adams, P.D. *et al.* PHENIX: building new software for automated crystallographic structure determination. *Acta Crystallogr. D Biol. Crystallogr.* **58**, 1948–1954 (2002).
56. McCoy, A.J. *et al.* Phaser crystallographic software. *J. Appl. Crystallogr.* **40**, 658–674 (2007).
57. Geertsma, E.R., Nik Mahmood, N.A., Schuurman-Wolters, G.K. & Poolman, B. Membrane reconstitution of ABC transporters and assays of translocator function. *Nat. Protoc.* **3**, 256–266 (2008).
58. Keller, S. *et al.* High-precision isothermal titration calorimetry with automated peak-shape analysis. *Anal. Chem.* **84**, 5066–5073 (2012).
59. Lorenz, C., Pusch, M. & Jentsch, T.J. Heteromultimeric CLC chloride channels with novel properties. *Proc. Natl. Acad. Sci. USA* **93**, 13362–13366 (1996).

doi:10.1038/nsmb.2904